



**HAL**  
open science

# Utilizing Iron as Reinforcement to Enhance Ambient Mechanical Response and Impression Creep Response of Magnesium

Subramanian Jayalakshmi, Seetharaman Sankaranarayanan, Ramachandra Arvind Singh, Rajashekhara Shabadi, Manoj Gupta

► **To cite this version:**

Subramanian Jayalakshmi, Seetharaman Sankaranarayanan, Ramachandra Arvind Singh, Rajashekhara Shabadi, Manoj Gupta. Utilizing Iron as Reinforcement to Enhance Ambient Mechanical Response and Impression Creep Response of Magnesium. *Metals*, 2021, *Metals*, 11 (9), pp.1448. 10.3390/met11091448 . hal-04414550

**HAL Id: hal-04414550**

**<https://hal.univ-lille.fr/hal-04414550>**

Submitted on 1 Feb 2024

**HAL** is a multi-disciplinary open access archive for the deposit and dissemination of scientific research documents, whether they are published or not. The documents may come from teaching and research institutions in France or abroad, or from public or private research centers.

L'archive ouverte pluridisciplinaire **HAL**, est destinée au dépôt et à la diffusion de documents scientifiques de niveau recherche, publiés ou non, émanant des établissements d'enseignement et de recherche français ou étrangers, des laboratoires publics ou privés.



Distributed under a Creative Commons Attribution 4.0 International License

Article

# Utilizing Iron as Reinforcement to Enhance Ambient Mechanical Response and Impression Creep Response of Magnesium

Subramanian Jayalakshmi <sup>1</sup>, Seetharaman Sankaranarayanan <sup>2,†</sup>, Ramachandra Arvind Singh <sup>1,\*</sup>, Rajashekhara Shabadi <sup>3,\*</sup> and Manoj Gupta <sup>2,\*</sup>

<sup>1</sup> School of Mechanical and Electrical Engineering, Wenzhou University, Wenzhou 325035, China; jayalakshmi.subramanian@gmail.com

<sup>2</sup> Department of Mechanical Engineering, National University of Singapore (NUS), Singapore 117576, Singapore; ssenseetharaman@yahoo.com

<sup>3</sup> UMET—Unité Matériaux et Transformations, CNRS, UMR 8207, Université de Lille, 59000 Lille, France

\* Correspondence: r.arvindsingh@gmail.com (R.A.S.); rajashekhara.shabadi@univ-lille.fr (R.S.); mpegm@nus.edu.sg (M.G.)

† Current address at Advanced Remanufacturing Technology Centre, ASTAR, Singapore 637143, Singapore.

**Abstract:** To realize light-weight materials with high strength and ductility, an effective route is to incorporate strong and stiff metallic elements in light-weight matrices. Based on this approach, in this work, magnesium–iron (Mg-Fe) composites were designed and characterized for their microstructure and mechanical properties. The Mg-Fe binary system has extremely low solubility of Fe in the Mg-rich region. Pure magnesium was incorporated with 5, 10, and 15 wt.% Fe particles to form Mg-Fe metal–metal composites by the disintegrated melt deposition technique, followed by hot extrusion. Results showed that the iron content influences (i) the distribution of Fe particles in the Mg matrix, (ii) grain refinement, and (iii) change in crystallographic orientation. Mechanical testing showed that amongst the composites, Mg-5Fe had the highest hardness, strength, and ductility due to (a) the uniform distribution of Fe particles in the Mg matrix, (b) grain refinement, (c) texture randomization, (d) Fe particles acting as effective reinforcement, and (e) absence of deleterious interfacial reactions. Under impression creep, the Mg-5Fe composite had a creep rate similar to those of commercial creep-resistant AE42 alloys and Mg ceramic composites at 473 K. Factors influencing the performance of Mg-5Fe and other Mg metal–metal composites having molybdenum, niobium, and titanium (elements with low solubility in Mg) are presented and discussed.



**Citation:** Jayalakshmi, S.; Sankaranarayanan, S.; Arvind Singh, R.; Shabadi, R.; Gupta, M. Utilizing Iron as Reinforcement to Enhance Ambient Mechanical Response and Impression Creep Response of Magnesium. *Metals* **2021**, *11*, 1448. <https://doi.org/10.3390/met11091448>

Academic Editor: Christine Borchers

Received: 14 August 2021

Accepted: 9 September 2021

Published: 13 September 2021

**Publisher's Note:** MDPI stays neutral with regard to jurisdictional claims in published maps and institutional affiliations.



**Copyright:** © 2021 by the authors. Licensee MDPI, Basel, Switzerland. This article is an open access article distributed under the terms and conditions of the Creative Commons Attribution (CC BY) license (<https://creativecommons.org/licenses/by/4.0/>).

**Keywords:** magnesium composites; iron particles; microstructure; mechanical properties

## 1. Introduction

Magnesium (Mg) alloys and Mg composites are prospective materials for automotive and aerospace industries [1,2], as they can significantly reduce the weight of structures due to their low density and high strength-to-weight ratio. Al, Zn, Zr, Mn, and rare earth metals are the elements commonly used for alloying Mg. To make Mg composites, usually ceramic particles (micron to nano-scale sizes) such as alumina, silicon carbide, boron carbide, boron nitride, and carbonaceous materials (e.g., carbon nanotubes and graphene) are incorporated as reinforcement to Mg matrices [3,4]. To achieve both high strength and ductility, metals that are strong, are stiff, and have a high melting point (e.g., Ti, Mo, Fe, Cr, and Nb) are potential reinforcements to make Mg-based composites, due in part to their limited solubility or no solid solubility with magnesium [5–10]. For example, incorporation of titanium in pure Mg to form Mg-5.6Ti improves tensile strength and ductility by 60% and 50% [5,6]. The addition of niobium and molybdenum to pure Mg has shown similar properties of improvement [6–9]. Sintered Mg-Ti composites have shown retention of their mechanical properties even at high temperatures [10].

Iron (Fe) is a low cost, high strength, and high melting point element. Iron has low solubility in magnesium, and the formation of magnesium–iron intermetallic compounds is absent [11,12]. There exists a eutectic reaction on the Mg-rich side at a temperature very close to the melting point of Mg; however, the composition of the eutectic point lies at <0.025 wt.% of Fe [12,13]. In the past, the presence of Fe in Mg (caused due to melting Mg in iron and steel crucibles) was considered as an impurity, as it drastically reduced the corrosion resistance of Mg [14]. However, a recent investigation [15] has found that Fe content even up to 25% in Mg-Fe does not lead to severe corrosion. Recent research has revealed that the addition of Fe to Mg is beneficial for applications related to biomedical implants [16,17], hydrogen sensing and storage [18,19], and electromagnetic shielding [20].

For high temperature performance such as creep resistance, the high temperature stability of materials is essential [4,21–23]. High temperature stability is important for powertrain components in automobile applications, e.g., engine components. At high operating temperatures, the coefficient of thermal expansion (CTE) is of concern as it affects the dimensional stability of components during service [24–26]. Mg–Al commercial alloys have better high temperature stability only for an Al content  $\leq 3\%$  [21]. An increase in Al content increases the formation of  $Mg_{17}Al_{12}$  intermetallic, and this phase degrades at temperatures  $>170\text{ }^{\circ}\text{C}$  (443 K), thus deteriorating mechanical performance [21–23]. A better elevated temperature performance of Mg materials has been achieved via making Al-free Mg alloys, by using rare earth (RE) metals as alloying elements, and by making Mg composites [23,27,28].

The Mg-Fe system does not form intermetallics, and Fe is inherently a high strength metal and has a high melting point (1811 K); hence, it is considered for investigation in the present work to assess its efficacy for applications that require high strength, high ductility, and high temperature stability. In this work, Mg-Fe metal–metal composites (Fe = 5, 10, and 15 wt.%) were synthesized by the disintegrated melt deposition technique and investigated for their microstructural characteristics and mechanical properties. A discussion on the performance of the composite that showed the best properties with those of Mg metal–metal composites containing other metallic elements such as titanium, niobium, and molybdenum [5–9] is also presented.

## 2. Experimental Details

### 2.1. Materials

Magnesium ingots of 99.8% purity (supplied by Tokyo Magnesium Company Limited, Yokohama, Japan) and iron particles of size 75 microns (98% purity, supplied by Alfa Aesar, Singapore) were used as the matrix and reinforcing materials, respectively.

### 2.2. Processing

Mg-Fe materials used in this study were synthesized through the liquid metallurgy route based disintegrated melt deposition (DMD) technique [1]. Mg turnings and Fe particles were heated in a graphite crucible to  $750\text{ }^{\circ}\text{C}$  in an electrical resistance furnace under inert argon gas protective atmosphere. The superheated molten slurry was stirred at 465 rpm using a twin blade (pitch  $45^{\circ}$ ) mild steel impeller (coated with Zirtex 25) for 5 min so as to facilitate uniform distribution of the Fe particles in molten Mg. The molten slurry was then bottom poured into a steel mould after disintegration by two jets of argon gas oriented normal to the melt stream. Following deposition, an ingot of 40 mm in diameter was obtained, which was then machined to a 36 mm diameter and soaked at  $400\text{ }^{\circ}\text{C}$  for 60 min. Hot extrusion was conducted using a 150 T hydraulic press at  $350\text{ }^{\circ}\text{C}$  with an extrusion ratio of 20.25:1, to obtain rods of 8 mm in diameter.

Synthesis of pure Mg was carried out using the steps mentioned above except that no reinforcement particles were added.

### 2.3. Testing and Characterization

#### 2.3.1. Density Measurements

Density measurements were conducted on polished samples taken from the extruded rods using Archimedes' principle. Distilled water was used as the immersion fluid. Weight measurements were made using an electronic balance (A&D HM-202, A&D Company, Limited, Tokyo, Japan) with an accuracy of  $\pm 0.1$  mg. Theoretical densities of composites were calculated using rule of mixtures. To determine their porosity, experimentally measured densities were compared with those of their theoretically estimated values. Porosity was calculated using the formula  $\text{Porosity (\%)} = [(\rho_{\text{Theoretical}} - \rho_{\text{Experimental}})/(\rho_{\text{Theoretical}} - \rho_{\text{air}})] \times 100$ , where  $\rho_{\text{air}}$  at 20 °C, and 1 atm is 0.0012 g/cm<sup>3</sup>.

#### 2.3.2. X-ray Diffraction

X-ray diffraction (XRD) analyses on the polished samples from extruded rods were performed using an automated Shimadzu LAB-XRD-6000 X-ray diffractometer (Shimadzu, Columbia, SC, USA) (Cu,  $K\alpha = 1.54056 \text{ \AA}$ ), with a scanning speed of 2°/min. Phase identification was carried out by matching the Bragg angle and the intensity of the peaks with the standard peaks of Mg, Fe, and other related phases. X-ray measurements were conducted on extruded samples, both in the transverse (i.e., sample cross-sectioned direction) and longitudinal directions to obtain information on bulk texture (i.e., crystallographic orientation) of Mg matrix.

#### 2.3.3. Microstructural Characterization

Microstructural characterization was conducted on the extruded pure Mg and Mg-Fe materials to examine the morphology of the grains and Fe particle distribution. Optical microscope (Olympus, Singapore, Singapore), Jeol JSM-5800 LV scanning electron microscope (Jeol SEM, JEOL Ltd., Tokyo, Japan), and field emission scanning electron microscope (Hitachi FESEM-S4300, Hitachi High-Technologies Corporation, Tokyo, Japan) coupled with energy dispersion analysis (EDS) were used for the characterization. Specimens for optical microscopy were sectioned, polished, and etched with citral (4.2 g of citric acid monohydrate in 100 mL of water) for 5 s at room temperature. Scion image analysis software was used to identify the average grain size and aspect ratio.

#### 2.3.4. Microhardness

Microhardness measurements were made on polished extruded samples using Matsuzawa MXT 50 automatic digital micro-hardness tester (Matsuzawa Co. Ltd., Tokyo, Japan). Tests were conducted in accordance with ASTM standard E3 84–99 using a Vickers indenter (test load: 25 gf; dwell time: 15 s). Three samples were tested for each composition. Ten to fifteen readings were taken, and the average values are reported.

#### 2.3.5. Tensile and Compressive Properties

Tensile and compression properties of the as-extruded pure Mg and Mg-Fe samples were evaluated using a fully automated servo-hydraulic mechanical testing machine (Model-MTS 810) (MTS Systems, Eden Prairie, MN, USA). For tensile tests, smooth bar tensile specimens with diameter 5 mm and gauge length 25 mm (in accordance with ASTM test method E8M-96) were used. The crosshead speed was set at 0.254 mm/min ( $1.69 \times 10^{-4} \text{ s}^{-1}$ ). For compression tests, samples with diameter of 8 mm and length to diameter ratio of  $l/d \sim 1$  obtained from the extruded rods were used as test specimens. The crosshead speed was set at 0.040 mm/s ( $8.3 \times 10^{-5} \text{ s}^{-1}$ ). For each composition, 5 tests were conducted, and the average values are reported.

#### 2.3.6. Fractography

Fracture surfaces of the tensile and compression tested samples were investigated using FESEM to identify the failure modes of the samples.

### 2.3.7. Coefficient of Thermal Expansion

Thermal expansion coefficient (CTE) of the extruded pure Mg and Mg-5Fe samples was conducted using an LINSEIS TMA PT 1000LT thermo-mechanical analyser (Linseis, Selb, Germany) at a heating rate of 5 °C/min. Argon gas flow rate was 100 ccm/min. Displacement of the test samples (each 5 mm long) as a function of temperature in the range 323 to 673 K was recorded using an alumina probe and was used to determine the CTE.

### 2.3.8. Impression Creep Tests

For impression creep tests, cylindrical samples with 6 mm diameter and 6 mm height were prepared from the extruded rods. Impression creep tests were carried out using an impression creep testing machine (Spranktronics, Bangalore, India), which contains constant-load equipment, a temperature controller, and a computer-controlled data acquisition system. In this method, by the application of a constant load (stress) at specific temperatures, the indenter is impressed on the sample. A tungsten carbide cylindrical punch (diameter: 1.5 mm) was used as the indenter. Indentation creep tests were performed under a load of 160 MPa and temperature of 473 K for dwell times up to 10,800 s (up to 3 h). During the load application, the impression depth was acquired as a function of time. Impression creep tests were performed on pure Mg and Mg-5Fe. For comparative study, impression creep tests were also conducted on Mg-5.6Ti and Mg-5.6Nb materials that were prepared by DMD method followed by hot extrusion [6,7].

## 3. Results and Discussion

### 3.1. Density and Porosity

The measured values and theoretical estimates of the density of pure Mg and Mg-Fe composites are given in Table 1. The porosities of Mg-Fe materials are higher than that of pure Mg. The porosity of the composites increased relative to the increase in Fe addition. The overall porosity for all the composites, however, remained <2%, indicating the near net shape forming capability of the processing methodology used in the present study.

**Table 1.** Density, porosity, and grain size of pure Mg and Mg-Fe composites.

Material	Density Measurements			Grain Size (µm)
	Theoretical Density (g/cm <sup>3</sup> )	Experimental Density (g/cm <sup>3</sup> )	Porosity (%)	
Pure Mg	1.7400	1.7393 ± 0.01	0.04	28 ± 9
Mg-5Fe	1.8274	1.8263 ± 0.01	0.06	13 ± 4
Mg-10Fe	1.9264	1.9195 ± 0.02	0.35	18 ± 3
Mg-15Fe	2.0368	2.0155 ± 0.03	1.04	20 ± 5

### 3.2. Microstructure and Phase Analysis

X-ray diffraction patterns for pure Mg and Mg-Fe materials, taken along the transverse and longitudinal directions of the extruded rods, are shown in Figures 1 and 2. Diffractograms show the presence of Mg peaks for the pure Mg sample and Mg and Fe peaks for Mg-Fe composites. No intermetallic phases and magnesium oxide peaks were identified. The absence of magnesium oxide peaks shows the capability of the fluxless and SF<sub>6</sub>-free DMD technique to mitigate the oxide formation solely using argon gas. The absence of intermetallic phase formation is due to the lack of solubility of Fe in Mg, as can be inferred from the Mg-Fe phase diagram [11–13].

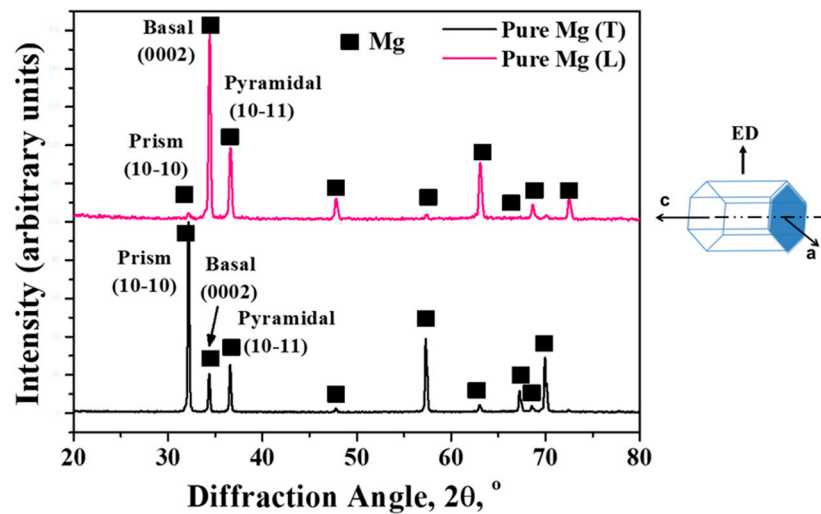


Figure 1. X-ray diffraction patterns of pure Mg along transverse and longitudinal sections.

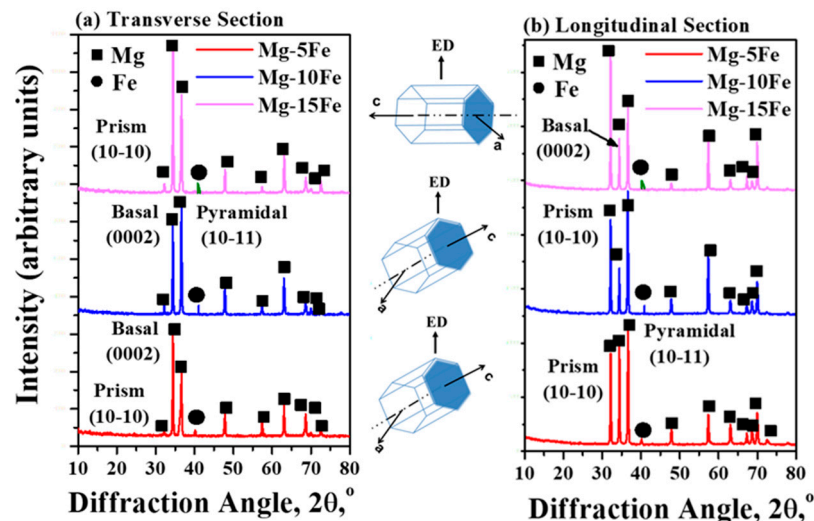
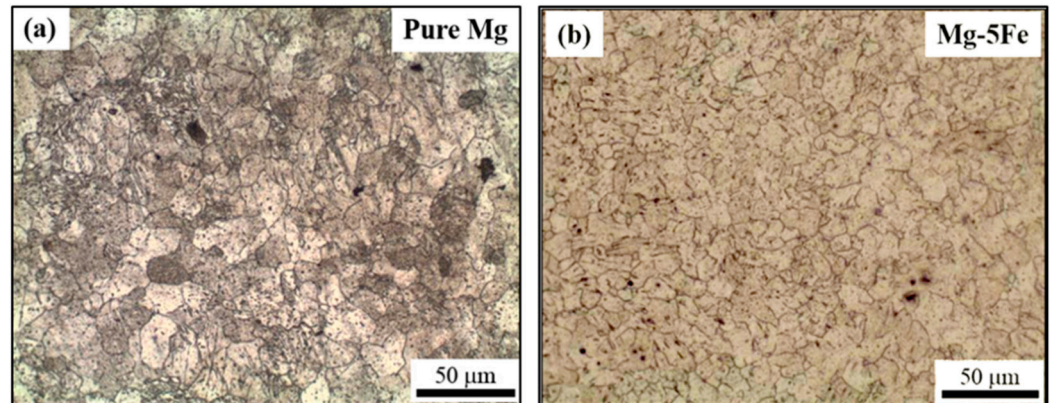


Figure 2. X-ray diffraction patterns of Mg-Fe composites along (a) transverse and (b) longitudinal sections.

Reinforcements and second phases can change the orientation (i.e., texture) of Mg matrices [29–31]. To understand the effect of Fe addition on the crystallographic orientation of the Mg matrix, X-ray analysis along the transverse and longitudinal sections was considered. Mg peaks observed at  $2\theta = 32^\circ$ ,  $34^\circ$ , and  $36^\circ$  diffraction patterns correspond to the (1 0–1 0) prism, (0 0 0 2) basal, and (1 0–1 1) pyramidal planes of the HCP Mg crystal (Figure 1). Along the transverse direction, the prismatic plane intensity ( $2\theta = 32^\circ$ ) is maximum for pure Mg and Mg-15Fe (Figure 2a), which is indicative of fibre texture (basal texture). This implies that the preferred alignment of prismatic planes in pure Mg and Mg-15Fe is in the direction perpendicular to their extrusion direction. Mg-5Fe and Mg-10Fe showed a maximum Mg peak intensity at  $36^\circ$ , which corresponds to the pyramidal planes (Figure 2a). For Mg-10Fe, the intensity of basal planes ( $2\theta = 34^\circ$ ) was found to be equally prominent as those of pyramidal planes. Along the longitudinal section, the intensity of basal planes ( $2\theta = 34^\circ$ ) is maximum for pure Mg, Mg-10Fe, and Mg-15Fe, whereas the intensity of pyramidal planes ( $2\theta = 36^\circ$ ) is maximum for Mg-5Fe. This observation shows a change in the bulk crystallographic orientation of Mg grains, caused by Fe addition, such that (i) the bulk texture change was not directly proportional to the amount of Fe addition and that (ii) pure Mg and Mg-15Fe have a fibre texture, whereas Mg-5Fe and Mg-10Fe have a randomized texture.

The measured grain size values of the test materials are given in Table 1. By the addition of Fe to Mg, the grain size decreased. As an example, the average grain size of Mg-5Fe decreased by >50% when compared to pure Mg (Figure 3). Grain refinement is due to Fe particles that act as obstacles and hinder grain growth via restricting the migration of grain boundaries during hot extrusion. The average grain size increases with increasing Fe content but still remains smaller than that of pure Mg.



**Figure 3.** Optical micrographs of (a) pure Mg and (b) Mg-5Fe.

The distribution of Fe particles in the Mg matrix is shown in Figure 4. Mg-Fe composites showed no interfacial reaction products and no interfacial debonding (e.g., Mg-5Fe, Figure 4a). In the Mg-5Fe composite, a uniform distribution of Fe particles was observed (Figure 4b). However, in Mg-10 Fe and Mg-15 Fe composites, Fe particles were found to be clustered (Figure 4c,d). The clustering of reinforcement particles in metal–metal composites has been observed earlier [6–9]. In the present work, the clustering of Fe particles in the Mg matrix (i) indicates that beyond a certain limit of Fe addition (in the present case 5%), agglomeration occurs due to the low solubility of Fe in Mg; (ii) leads to an increase in the porosity level (cluster-associated porosity due to inefficient packing of Fe particles, Table 1); and (iii) does not effectively enable grain nucleation and, thereby, the relatively larger grain sizes seen in Mg-10 Fe and Mg-15 Fe when compared to Mg-5Fe (Table 1).

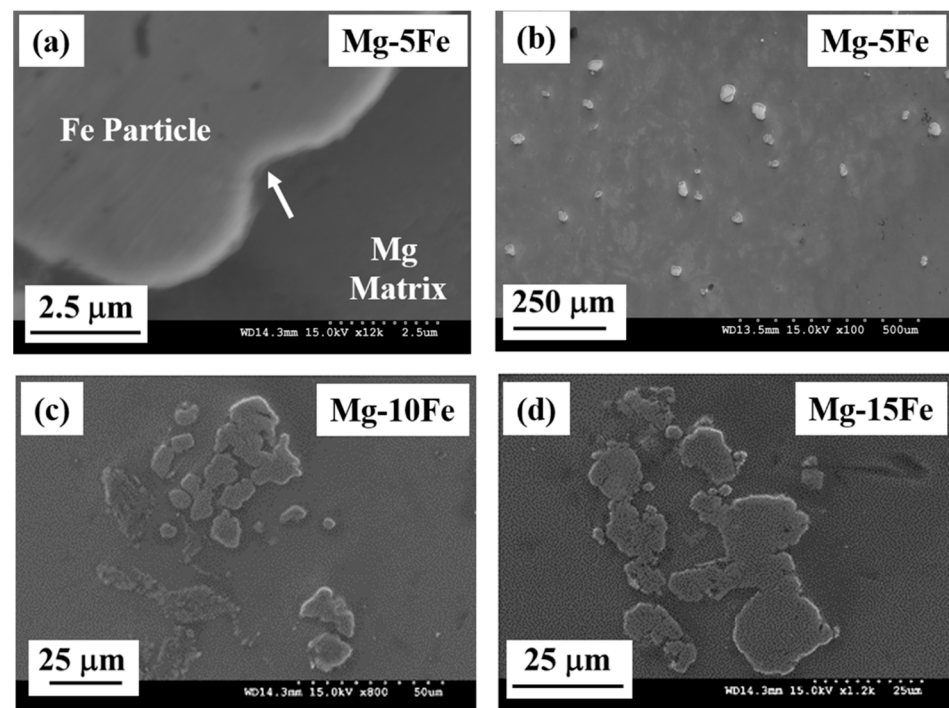


**Figure 4.** SEM micrographs: (a) clear interface in Mg-5Fe (shown by the arrow). No interfacial reaction products at interface. Distribution of Fe particles in Mg-matrix: (b) Mg-5Fe; (c) Mg-10Fe; and (d) Mg-15Fe.

### 3.3. Mechanical Properties

#### 3.3.1. Microhardness

Microhardness values of pure Mg and Mg-Fe materials are given in Table 2. All Mg-Fe materials have a higher hardness than pure Mg, which is due to Fe particles. Fe has a hardness value of  $\approx 150$  Hv [32], which is almost four times that of Mg (42.4 Hv, Table 2). Fe can be considered as metallic reinforcement to Mg, as it does not form any intermetallic phase with Mg and increases the hardness. The presence of hard Fe particles in the Mg matrix causes a higher constraint to localized matrix deformation during indentation, resulting in a higher hardness [33,34]. However, it is seen that the percentage increase in hardness value of Mg-Fe composites decreases with the increase in Fe content, such that (i) a 5% addition of Fe increased the hardness value by  $>50\%$ , (ii) a 10% addition of Fe increased the hardness value by  $>30\%$ , and (iii) a 15% addition of Fe increased the hardness value by  $>10\%$ , when compared to pure Mg. This decreasing trend in hardness with an increase in Fe content is attributed to (a) an increase in porosity level in the composites with an increase in Fe content (Table 1) and (b) non-uniform matrix hardening due to clustering of Fe particles in Mg-10Fe and Mg-15Fe composites (Figure 4). Amongst Mg-Fe composites, the Mg-5Fe composite displayed the highest microhardness.

**Table 2.** Microhardness values of pure Mg and Mg-Fe composites.

Material	Microhardness (Hv)
Pure Mg	$42.4 \pm 1.8$
Mg-5Fe	$64.4 \pm 2.8$
Mg-10Fe	$56.0 \pm 3.4$
Mg-15Fe	$49.4 \pm 3.6$

#### 3.3.2. Tensile Properties

The tensile properties of pure Mg and Mg-Fe composites are given in Table 3. Engineering stress–strain curves of pure Mg and Mg-Fe composites under tensile loading are

shown in Figure 5. All Mg-Fe composites have a higher tensile yield strength (TYS), higher ultimate tensile strength (UTS), and higher% elongation (except for Mg-15Fe) than pure Mg, which is due to the presence of Fe particles. Fe particles act as metallic reinforcement and provide strengthening by efficient load transfer from the matrix to reinforcement [35,36]. The tensile properties and ductility of Mg-Fe composites in comparison to those of pure Mg were such that (i) for Mg-5Fe, yield strength and ultimate strength increased by 28% and 34%, respectively, and ductility by 57%; (ii) for Mg-10Fe, yield strength and ultimate strength increased by 12% and 28%, respectively, and ductility by 25%; and (iii) for Mg-15Fe, yield strength increased by 7.5%, and ultimate tensile strength was retained, whereas the ductility decreased by 60%. Mg-5Fe displayed the highest tensile properties.

**Table 3.** Tensile properties of pure Mg and Mg-Fe composites.

Material	0.2 Tensile Yield Strength (MPa)	Ultimate Tensile Strength (MPa)	Elongation (%)
Pure Mg	120 ± 9	160 ± 11	6.4 ± 0.7
Mg-5Fe	154 ± 3	215 ± 6	10.1 ± 0.7
Mg-10Fe	135 ± 8	205 ± 5	8.04 ± 0.2
Mg-15Fe	129 ± 9	161 ± 15	2.6 ± 0.6

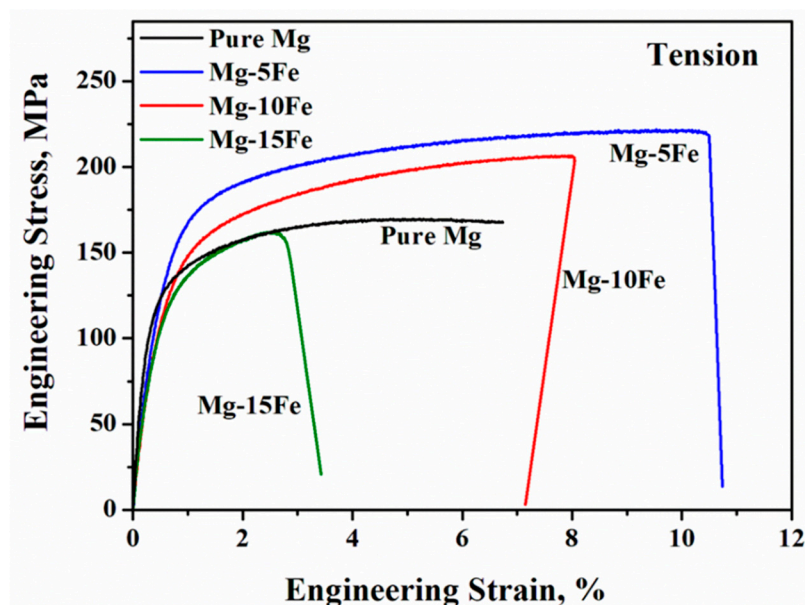


**Figure 5.** Tensile stress–strain curves of pure Mg and Mg-Fe composites.

Despite the lack of solid solubility between Mg and Fe, the ductility (i.e., strain to failure, % elongation) improvement in the composites can be attributed to (i) good mechanical bonding between Fe particles and the Mg matrix and (ii) the dissipation of stress concentration present at the crack front by Fe particles [37,38]. However, a drastic reduction in ductility of Mg-15Fe is mainly due to the severe clustering of Fe particles in the composite (Figure 4d). Such clustering of particles aids void nucleation and growth [39], as clusters have a high-volume fraction of particles when compared to the surrounding zones. A high localised volume fraction of particles leads to increased stress concentration in the clustered zone and thereby voids initiate under tensile loading conditions and propagate as cracks. For uniform deformation to occur, the high stress concentration regions activate additional slip systems to accommodate the same amount of deformation vis à vis the surrounding matrix, which causes fracture at particle clusters, thereby leading to the premature failure of material [40,41]. Furthermore, the high porosity level in Mg-15Fe (Table 1) accelerates failure. As seen from Figure 5, for all the materials, the engineering stress–strain curves after their yield points show low work hardening until fracture. This

behaviour of higher yield stress and low work hardening is primarily due to basal slip [5,42], and activation of non-basal slip systems as twinning is not favoured under tension [42,43]. The deformation behaviour under tension is hence slip dominant.

### 3.3.3. Compressive Properties

The compressive strength properties of pure Mg and Mg-Fe composites are given in Table 4. Engineering stress–strain curves of pure Mg and Mg-Fe composites under compressive loading are shown in Figure 6. All Mg-Fe composites have a higher compressive yield strength (CYS) and a higher ultimate compressive strength (CTS) than pure Mg, which is due to the presence of Fe particles. The compressive strength properties of Mg-Fe composites in comparison to those of pure Mg were such that (i) for Mg-5Fe, the yield strength and ultimate strength increased by 53% and 32%, respectively; (ii) for Mg-10Fe, the yield strength and ultimate strength increased by 23% and 5.5%, respectively; and (iii) for Mg-15Fe, the yield strength increased by 12%, and the ultimate compressive strength was retained. The compressive ductility of Mg-5Fe increased slightly by 4%, whereas for Mg-10Fe and Mg-15Fe, the compressive ductility decreased by 11% and 22%, respectively. Amongst the Mg-Fe composites, the Mg-5Fe composite displayed the highest compressive properties. As seen from Figure 6, for all the materials, the engineering stress–strain curves have a sigmoidal shape with an initial upward concave profile (after their yield points) and a subsequent convex profile. As opposed to under tension, significant work hardening under compression in extruded Mg materials is due to deformation by twinning [42,43]. Furthermore, the activation of non-basal slip systems also contributes to work hardening [42], and as a result, the overall compressive strength (with large strains) increases.

**Table 4.** Compression properties of pure Mg and Mg-Fe composites.

Material	0.2 Compressive Yield Strength (MPa)	Ultimate Compressive Strength (MPa)	Failure Strain (%)
Pure Mg	65 ± 1	305 ± 5	19.5 ± 7.2
Mg-5Fe	100 ± 4	403 ± 23	20.3 ± 8.2
Mg-10Fe	80 ± 3	322 ± 29	17.1 ± 2.3
Mg-15Fe	73 ± 2	310 ± 38	15.1 ± 3.8

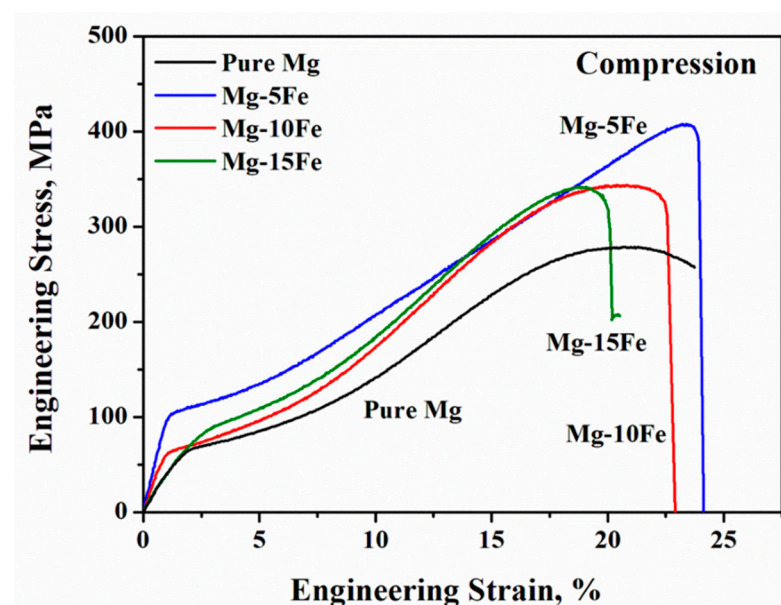


**Figure 6.** Compression stress–strain curves of pure Mg and Mg-Fe composites.

### 3.3.4. Fractography

Fractography of tensile tested samples (Figure 7) indicates the failure mode of samples. Dominant ductile fracture features were observed in Mg-5Fe (Figure 7a), which showed high ductility (Figure 5). Mixed mode fracture with ductile and brittle features was observed for Mg-10Fe (Figure 7b). Fe particles remained intact in the Mg matrix, and debonding from the Mg matrix was not observed for composites (e.g., Mg-10Fe, Figure 7c). In Mg-15Fe, particle cracking was observed, with dominant brittle fracture features (Figure 7d).

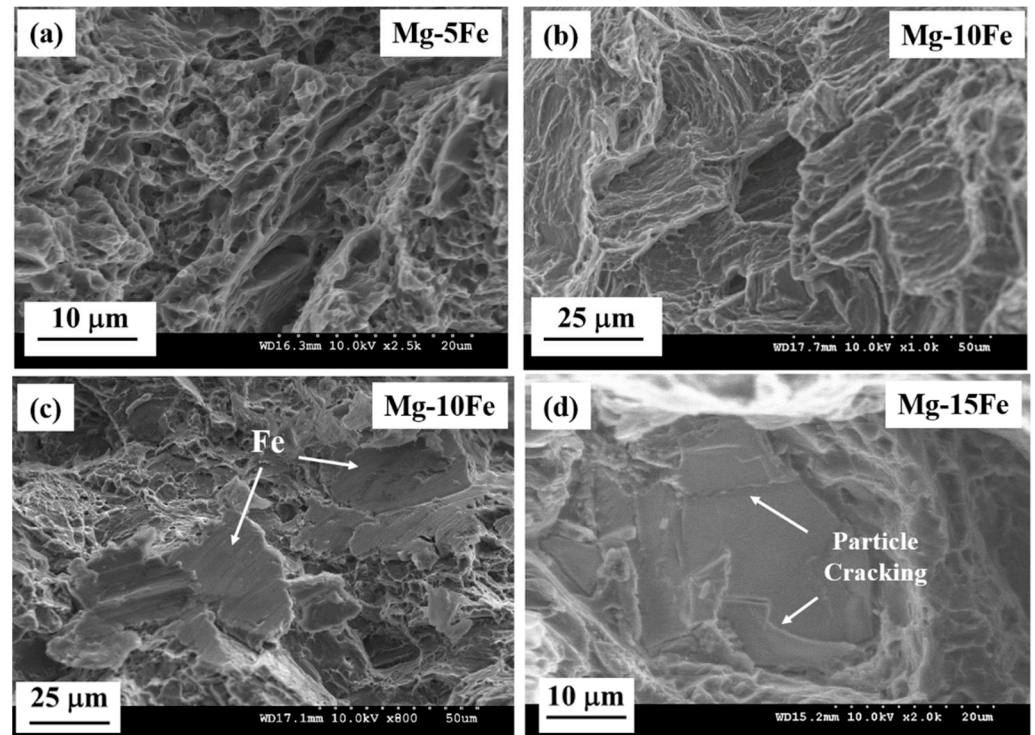


**Figure 7.** SEM fractography of tensile tested samples: (a) Mg-5Fe; (b) Mg-10Fe; (c) Mg-10Fe showing Fe particles remaining intact without debonding; and (d) particle cracking in Mg-15Fe.

SEM micrographs of fractured compression test samples are shown in Figure 8a–d. For all the samples, fracture occurred at  $\sim 45^\circ$  angle with respect to the compression test axis. The presence of shear bands indicates that all composites experienced shear failure. Mg-10Fe and Mg-15Fe (Figure 8b,c) show rough fracture surfaces with a mixed mode of shear and brittle features. Scoring marks on Mg-15Fe (shown by arrows) caused by Fe particle clusters during matrix shearing can be seen in Figure 8d.

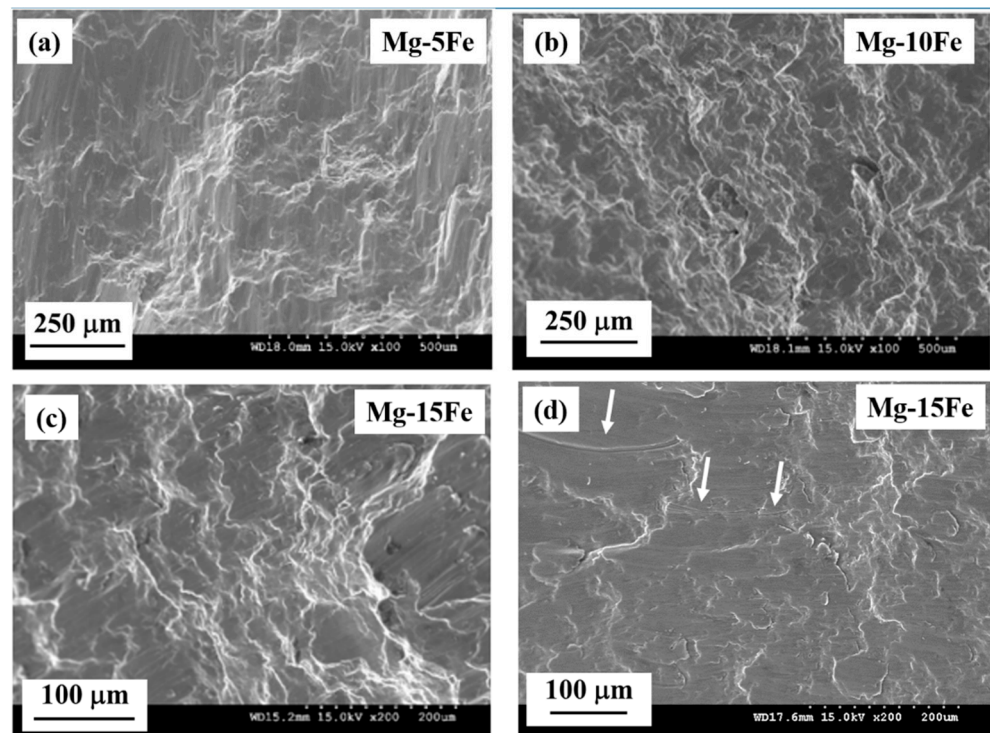


**Figure 8.** SEM fractography of compression tested samples showing shear fracture: (a) Mg-5Fe; (b) Mg-10Fe; and (c) Mg-15Fe; (d) Scoring marks on Mg-15Fe (shown by arrows) caused by Fe particle clusters during matrix shearing.

### 3.4. Coefficient of Thermal Expansion

The coefficient of thermal expansion is (CTE) is a thermo-physical property that influences the dimensional stability of materials at elevated temperatures. The measured thermal expansion coefficient values of pure Mg and the Mg-5Fe composite are given in Table 5. The composite has a lower CTE value than pure Mg, which implies that the Mg-5Fe composite can retain better dimensional stability at elevated temperatures. The lower CTE value of the composite is primarily due to the contribution by Fe particles that have a lower CTE value (CTE value of Fe:  $11.8 \times 10^{-6}/\text{K}$ ) than pure Mg (CTE value of Mg:  $28.4 \times 10^{-6}/\text{K}$ ) [44]. The Mg-5Fe composite has a lower CTE value than those of some of the existing high temperature resistant Mg alloys such as QE22, AS21, EZ33, Mg-Sn, and other Mg metal–metal systems such as Mg-5.6Ti and Mg-3.6Mo [5,7,26,44–46] (Table 5). Although Ti and Mo have CTE values lower than Fe, the CTE values of Mg-5.6Ti and Mg-3.6Mo composites are slightly higher than that of Mg-5Fe, probably due to the clustering of Ti and Mo particles [6,7].

**Table 5.** Coefficient of thermal expansion values of pure Mg, Mg-5Fe, Mg-Ti, Mg-Mo, and high temperature resistant Mg alloys [6,7,26,45,46].

Material	Coefficient of Thermal Expansion, CTE ( $\times 10^{-6}/\text{K}$ )
Pure Mg	$28.52 \pm 0.12$
Mg-5Fe (Present Work)	$26.71 \pm 0.37$
Mg-5.6Ti [6]	27.22
Mg-3.6Mo [7]	27.8
Mg-5Sn [45]	27.4
QE22 [46]	26.7
AS21 [46]	27.0
EZ33 [46]	26.8

### 3.5. Impression Creep Behaviour

Impression creep curves of Mg-5Fe at 160 MPa and at 473 K are shown in Figure 9. The figure also shows creep curves for pure Mg, Mg-5.6Ti, and Mg-5Nb. Impression depth as a function of time is shown for the materials in Figure 9a. These materials experience primary creep, i.e., an increase in creep with time, followed by secondary creep, wherein their creep reached steady state. Fracture of samples (i.e., tertiary creep) does not occur in impression creep tests. During the creep process, materials experience work hardening and recovery [21]. Steady state is attained when an equilibrium is reached between these two competing mechanisms [21]. As can be seen from Figure 9a, the impression depth with respect to time is relatively lower for Mg-5Fe than that of pure Mg. Furthermore, Mg-Ti has the least penetration depth, and Mg-Nb has the highest penetration depth.

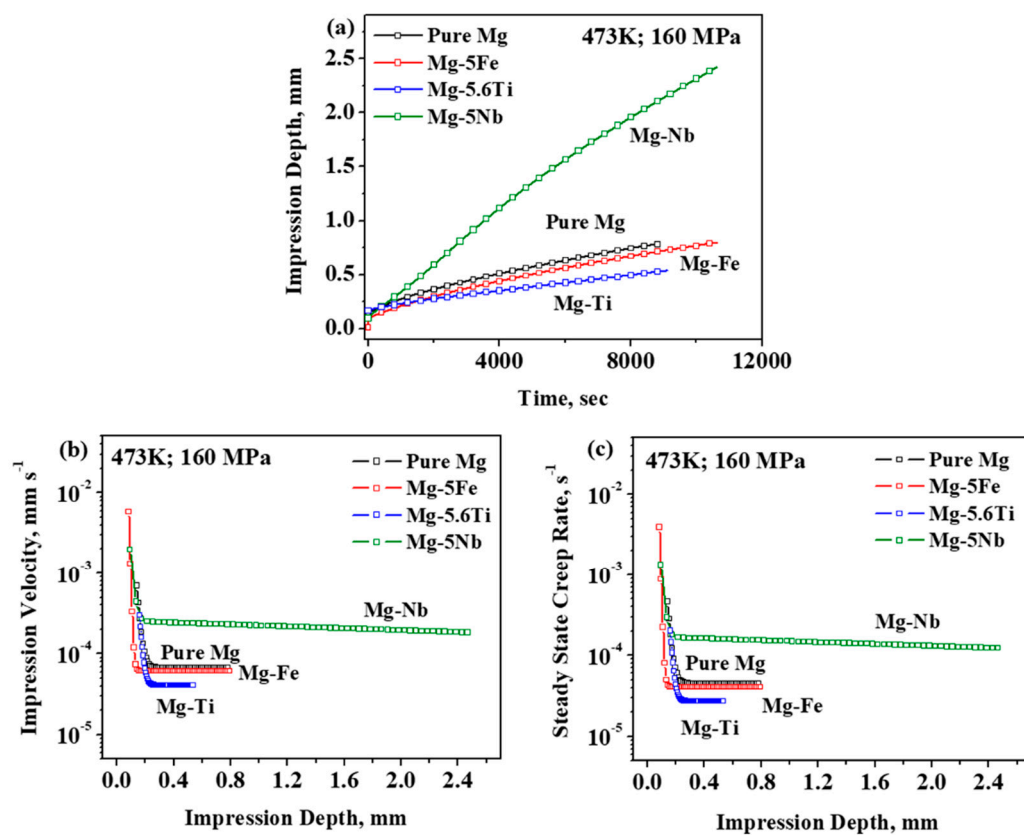


**Figure 9.** Impression creep curves of pure Mg, Mg-5Fe, Mg-5.6Ti, and Mg-5Nb: (a) Variation of impression depth vs. time; (b) variation of impression velocity with impression depth; and (c) steady state creep rate of the materials.

The impression velocity of the materials (change in impression depth with time,  $V_{\text{imp}} = dh/dt$ ) as a function of impression depth is shown in Figure 9b. Steady states are reached when  $V_{\text{imp}}$  for the materials becomes constant with depth. Steady state creep rate values are obtained by plotting  $V_{\text{imp}}/2a$  (minimum creep rate), where  $V_{\text{imp}}$  is the impression velocity, and  $2a$  is the diameter of the indenter (Figure 9c) [47,48]. From the figure, it is seen that the steady state creep rate of Mg-5Fe is relatively lower than that of pure Mg. Contradictory results on the enhancement of creep resistance of Mg composites with ceramic reinforcements have been reported earlier. While Mg-SiC particle composites and AE42 hybrid composites have shown higher creep resistance (i.e., lower creep rate) than their unreinforced counterparts [27,49], QE22-SiC composites had lower creep resistance than the alloy, due to increased grain boundary sliding and particle/matrix interfacial sliding in the composites [50,51]. In the present case, the steady state creep rate of Mg-5Fe

is slightly lower than pure Mg. Mg-5.6Ti has a lower creep rate than that of Mg-5Fe, and the creep rate of Mg-5Nb is 3.25 times higher than that of Mg-5Fe.

Mg materials have lower creep rates (i.e., higher creep resistance) than Al materials. Lower creep rates in Mg materials are due to the high internal stress of the hcp. structure (with only two independent basal slip systems), when compared to the fcc. structure of Al materials [52]. Pure Mg is known to creep by lattice self-diffusion [53]. Studies on the impression creep behaviour of creep resistant Mg alloys and Mg composites have reported that the materials undergo creep via dislocation climb controlled by a pipe diffusion mechanism (at the temperature and applied stress as used in the present work; 473 K and 160 MPa) [27,48,49,54]. In Mg-5Fe, Fe is a strong, stiff, and high melting point element and thus can impede dislocation motion in the Mg matrix. For dislocation motion to continue, dislocations have to overcome obstacles. At a high temperature, this occurs by dislocation climb via changing of slip planes assisted by vacancy transport [55,56]. In the present work, the test temperature of 473 K is  $>0.5 T_m$  of the Mg matrix, which would facilitate vacancy movement and transport, and thereby dislocations climb over obstacles (here, Fe particles). It is hence reasonable to suggest that the creep mechanism in Mg-5Fe would predominantly occur by dislocation climb controlled by pipe diffusion.

### 3.6. Factors Influencing Performance of Mg Composites

#### 3.6.1. Microstructure

Distribution of reinforcement particles in the matrix is an important microstructural feature that determines load transfer from the matrix to particles. In the Mg-Fe composites, for Fe content  $> 5$  wt.%, clustering of particles occurred that reduced their strength properties. Furthermore, a change in crystal orientation with increasing Fe content was identified using XRD analysis (Figure 2). Mg materials deform by basal slip which is the dominant deformation mechanism based on the lower critical resolved shear stress (CRSS) value at room temperature [30,31,43]. Pure Mg and Mg-15Fe have a characteristic fibre texture with {0002} planes perpendicular to the extrusion direction, which reduces their ductility. Texture randomization (i.e., weakening) in Mg-5Fe and Mg-10Fe composites is favourable for slip transition to occur (basal to non-basal/cross slip), which improves their ductility. However, due to clustering of Fe particles in Mg-10Fe, its ductility was lower than that of Mg-5Fe.

#### 3.6.2. Reinforcing Metallic Elements

Nature (i.e., ceramic or metallic) and morphology (i.e., shape and size) of the reinforcing phase in the Mg matrix influence the material response to externally applied loading conditions. Ceramic reinforcements usually cause interfacial reactions at the reinforcement/matrix interface [3,57] that drastically reduce ductility. Reinforcing metallic particles with no or minimal solubility in Mg shows no interfacial products, as seen in Mg-Fe (Figure 4a), Mg-Ti, Mg-Nb, and Mg-Mo composites [5–9]. The absence of any deleterious interfacial products leads to efficient load transfer from the matrix to reinforcement, thereby enhancing strength and ductility (Tables 3 and 4). Hardness, tensile, and compressive properties of Mg-5Fe (the composite that has shown the best performance) and Mg composites having other metallic reinforcements are given in Tables 6 and 7. On a comparative note, the Mg-5Fe outperforms Mg metal–metal composites with other metallic reinforcements in terms of strength and ductility improvement, the reasons being: (i) the uniform distribution of Fe particles without clustering, (ii) random texture evolution, and (iii) Fe particles with rounded corners (i.e., particle corners are not sharp). Some reasons as to the relative lower performance of Mg metal–metal composites with other metallic reinforcements are (i) Mg-5.6Ti, Mg-3.6Mo, and Mg-5Nb had clustered particles [6–8], and (ii) Ti particles in Mg-5.6Ti were irregular in shape with sharp corners and were large in size ( $<140 \mu\text{m}$ ) [6]. Usually, irregularly shaped particles with sharp corners increase dislocation density, which would contribute towards strength improvement. However, they would also aid clustering, which would reduce the ductility of materials (as was observed in

Mg-5.6Ti, [6]). In addition, (iii) the strong basal texture in Mg-5.6Ti was unfavourable in terms of ductility [58]. Compared to the rest of the Mg metal–metal composites, Mg-5Nb showed the highest ductility, as Nb is an inherently ductile metal (~50% elongation at room temperature) [59].

**Table 6.** Hardness and tensile properties of Mg-5Fe and Mg composites having other metallic reinforcements [6–8].

Material	Micro Hardness HV	TYS MPa	UTS MPa	% Elongation	Property Comparison of Mg-5Fe with Data in the Literature [% Increase (+) or Decrease (–)]
Mg-5Fe [Present Work]	64.4	154	215	10.1	–
Mg-5.6Ti [6]	71	158	226	8.0	(–) 9.5% Hv (–) 2.5% TYS and 5.1% UTS (+) 26.5% Elongation
Mg-3.6Mo [7]	61.6	123	197	9	(+) 7% Hv (+) 25% TYS and (+) 9% UTS, (+) 12% Elongation
Mg-5Nb [8]	45	129	186	13.0	(+) 42% Hv (+) 19% TYS, (+) 15.5% UTS, (–) 28% Elongation

**Table 7.** Compression properties of Mg-5Fe and Mg composites having other metallic reinforcements [6,8].

Material	CYS MPa	UCS MPa	Ductility	Property Comparison with Data in the Literature [% Increase (+) or Decrease (–)]
Mg-5Fe [Present Work]	100	403	20.3	–
Mg-5.6Ti [6]	80	360	13.6	(+) 25% CYS, (+) 11% UCS (+) 49% Ductility
Mg-5Nb [8]	75	290	22.4	(+) 33% CYS, (+) 38% UCS (–) 10.3% Ductility

### 3.6.3. Strengthening Mechanisms

Strengthening effects that contribute towards the enhancement of the tensile and compressive strength of Mg-Fe composites are [35,36,57,60–64]: (i) particle strengthening by the presence of strong and stiff Fe particles, which increases load carrying capacity; (ii) an increase in dislocation density due to thermal residual stresses, which arises due to the difference in the CTE values of the matrix (Mg:  $28.4 \times 10^{-6}/\text{K}$ ) and particles (Fe:  $11.8 \times 10^{-6}/\text{K}$ ) and increases yield strength; (iii) the Hall–Petch effect of increase in yield strength due to grain refinement; (iv) Orowan strengthening due to the hindrance of dislocation motion by Fe particles; and (v) texture randomization that activates non-basal slip planes, which enhances the work hardening ability. These mechanisms also improve tensile and compressive properties in other Mg metal–metal composite systems such as Mg-Ti, Mg-Nb, and Mg-Mo [6–8].

Figure 10 shows steady state creep rate values of Mg-5Fe (shown by arrow) in comparison with those of Mg-5.6 Ti, Mg-5Nb, Mg alloys (AZ31, Mg-5Sn, AE42 [27,48]), Mg composites with ceramic reinforcements (Mg-SiC [49]), and Al alloys (A356, A356 + Sc [65]). Data for Mg alloys, Mg composites with ceramic reinforcements, and Al alloys were referred to from published reports. The data referred to for these materials are from impression creep tests conducted at the same temperature and stress as used in the present work (473 K; 160 MPa). Dominant creep strengthening mechanisms for the different material systems are mentioned in the figure.

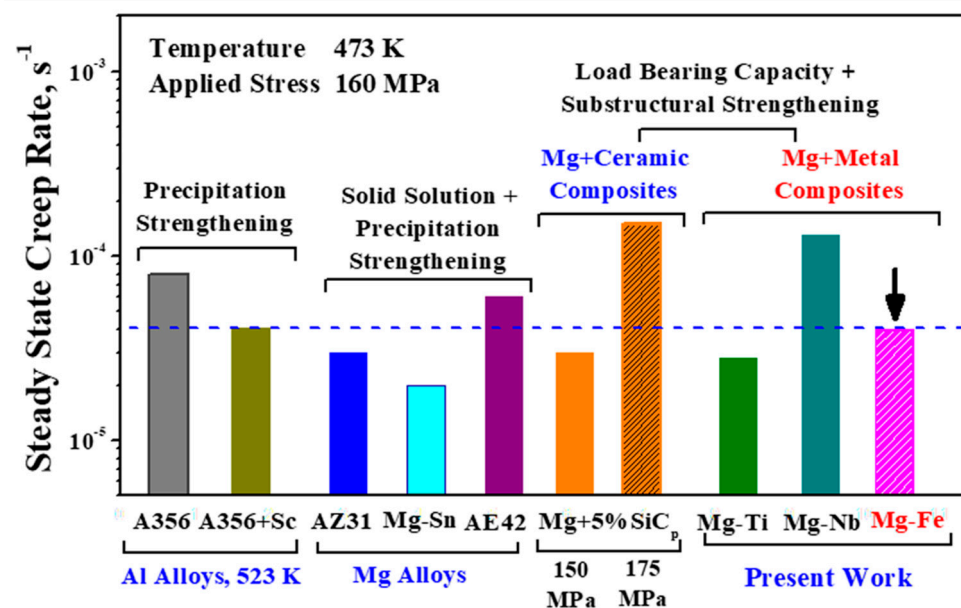


**Figure 10.** Steady state creep rate of Mg-5Fe (shown by arrow), Mg-5.6 Ti, Mg-5Nb, Mg alloys [27,48], Mg composites with ceramic reinforcements [49], and Al alloys [65]. Data for Mg alloys, Mg composites with ceramic reinforcements, and Al alloys were referred to from published reports. The data referred to for these materials are from impression creep tests conducted at the same temperature and stress as used in the present work (473 K; 160 MPa). Dominant creep strengthening mechanisms for the different material systems are mentioned.

Mg materials inherently have lower creep rates when compared to Al materials [49]. In most of the Mg alloys, creep strengthening occurs due to solid solution, precipitation, grain boundaries, and dislocation hardening [21,27,48,52,53]. Solid solution strengthening is the dominant mechanism in the commercial AZ31 alloy. In Mg-Al alloys, at a temperature >443 K,  $Mg_{17}Al_{12}$  precipitates undergo dissolution, and hence precipitation strengthening is absent. Precipitation strengthening is the dominant creep strengthening mechanism in creep resistant Mg alloys (Mg-5Sn and AE42), wherein the presence of thermally stable precipitates such as the  $Mg_2Sn$  phase in Mg-5Sn and the rare earth metal based precipitate phase in the AE42 alloy improve their creep resistance [27,48]. In Mg composites, the major strengthening mechanisms are: (i) the load bearing capacity by hard reinforcement particles and (ii) substructural strengthening. Substructural features that provide strengthening include: (i) grain refinement, (ii) type (e.g., fibre, particles) and distribution of reinforcement, (iii) increase in dislocation density, and (iv) formation of twins. Dislocation hardening arises due to CTE mismatch and due to the pinning of dislocations by reinforcements. For example, in Mg-SiC<sub>p</sub> composites, strengthening predominantly occurs due to dislocation hardening and grain boundary strengthening [49].

Solid solution strengthening and precipitation strengthening do not occur in Mg-5Fe, Mg-5.6Ti, and Mg-5Nb, which is due to a lack of solubility between Mg and metallic reinforcements. Rather, mechanisms that contribute to creep strengthening include:

- (i) Load bearing effect, due to metallic reinforcements that are strong and thermally stable.
- (ii) Dislocation hardening, due to CTE mismatch between Mg and its metallic reinforcements.
- (iii) Particle strengthening, due to uniform distribution of Fe particles in Mg, for the case of Mg-5Fe. In the case of Mg-Ti, the irregularly shaped and sharp-cornered reinforcement Ti particles increase dislocation density in the matrix. Mg-5.6Ti has the lowest creep rate amongst the Mg metal-metal composites.
- (iv) Orowan strengthening, due to the effective pinning of dislocations by metallic reinforcements.

In addition to the above-mentioned mechanisms, the interaction of twins with grain boundaries would lead to back stress and pile-up within grains and also contributes to the creep strengthening of the materials [66].

#### 4. Conclusions

Magnesium composites containing iron particles (Fe = 5, 10 and 15 wt.%) were synthesized using a disintegrated melt deposition technique followed by hot extrusion. Microstructure and mechanical properties were investigated. The following are the conclusions that could be drawn from the present study:

- Addition of Fe particles to the Mg matrix resulted in a metal–metal composite, due to a lack of solid solubility between Mg and Fe. Fe particles act as metallic reinforcement in the Mg matrix.
- Fe content influences grain refinement, uniform distribution of Fe particles, and crystallographic orientation of the Mg matrix.
- Addition of Fe to Mg significantly improves mechanical properties. Amongst the Mg-Fe composites, Mg-5Fe showed the best hardness, tensile, and compression strength properties, with significant improvement in ductility. Mg-5Fe has better dimensional stability and a lower creep rate when compared to the commercial AE42 alloy and Mg-SiC composite.
- Mg-5Fe showed the best mechanical performance due to (a) a uniform distribution of Fe particles in the Mg matrix, (b) grain refinement, (c) texture randomization, (d) Fe particles acting as effective reinforcement and contributing to various strengthening mechanisms, and (e) the absence of deleterious interfacial reactions.

Mg-Fe composites, due to their high strength, ductility, and high temperature stability, can be considered for aerospace, automotive, and biomedical applications. Compared to other metallic reinforcement elements, such as Ti, Mo, Nb, etc., Fe is relatively less expensive and would provide cost effectiveness for bulk manufacturing.

**Author Contributions:** Conceptualization, S.J., S.S. and M.G.; methodology, S.J. and S.S.; software, S.J. and S.S.; validation, S.J. and S.S.; formal analysis, S.J. and S.S.; investigation, S.J. and S.S.; resources, S.J., M.G., R.A.S. and R.S.; data curation, S.J. and S.S.; writing—original draft preparation, S.J.; writing—review and editing, S.J., S.S., R.A.S., M.G. and R.S.; visualization, S.J., S.S., R.A.S., M.G. and R.S.; supervision, S.J. and M.G.; project administration, S.J., S.S. and M.G. All authors have read and agreed to the published version of the manuscript.

**Funding:** This research received no external funding.

**Institutional Review Board Statement:** Not applicable.

**Informed Consent Statement:** Not applicable.

**Data Availability Statement:** Not applicable.

**Conflicts of Interest:** The authors declare no conflict of interest.

#### References

1. Vicenzi, B.; Boz, K.; Aboussouan, L. Powder metallurgy in aerospace—fundamentals of pm processes and examples of applications. *Acta Met. Slovaca* **2020**, *26*, 144–160. [[CrossRef](#)]
2. Kondo, H.; Hegedus, M. Current trends and challenges in the global aviation industry. *Acta Met. Slovaca* **2020**, *26*, 141–143. [[CrossRef](#)]
3. Gupta, M.; Sharon, N.M.L. *Magnesium, Magnesium Alloys, and Magnesium Composites*; John Wiley & Sons: Hoboken, NJ, USA, 2011.
4. Kainer, K. *Metal Matrix Composites: Custom-Made Materials for Automotive and Aerospace Engineering*; John Wiley & Sons: Oxford, UK, 2006.
5. Hassan, S.; Gupta, M. Development of ductile magnesium composite materials using titanium as reinforcement. *J. Alloys Compd.* **2002**, *345*, 246–251. [[CrossRef](#)]
6. Sankaranarayanan, S.; Jayalakshmi, S.; Gupta, M. Effect of addition of mutually soluble and insoluble metallic elements on the microstructure, tensile and compressive properties of pure magnesium. *Mater. Sci. Eng. A* **2011**, *530*, 149–160. [[CrossRef](#)]

7. Wong, W.L.E.; Gupta, M. Enhancing thermal stability, modulus and ductility of magnesium using molybdenum. *Adv. Eng. Mater.* **2005**, *7*, 250–255. [[CrossRef](#)]
8. Shanthi, M.; Jayaramanavar, P.; Vyas, V.; Seenivasan, D.; Gupta, M. Effect of niobium particulate addition on the microstructure and mechanical properties of pure magnesium. *J. Alloys Compd.* **2012**, *513*, 202–207. [[CrossRef](#)]
9. Subramanian, J.; Loh, Z.; Seetharaman, S.; Hamouda, A.S.; Gupta, M. Microstructure and Mechanical Properties of Mg-5Nb Metal-Metal Composite Reinforced with Nano SiC Ceramic Particles. *Metals* **2012**, *2*, 178–194. [[CrossRef](#)]
10. Perez, P.; Garcés, G.; Adeva, P. Mechanical properties of a Mg–10 (vol.%)Ti composite. *Comp. Sci. Tech.* **2004**, *64*, 145–151. [[CrossRef](#)]
11. von Goldbeck, O.K. *Iron-Magnesium Fe-Mg: Iron-Binary Phase Diagrams*; Springer: Berlin/Heidelberg, Germany, 1982; Chapter 37; pp. 59–60.
12. Nayeb-Hashemi, A.A.; Clark, J.B.; Swartzendruber, L.J. The Fe-Mg (Iron-Magnesium) System. *Bull. Alloy Phase Diag.* **1985**, *6*, 235–238. [[CrossRef](#)]
13. Yue, A.S. The magnesium-iron eutectic and the maximum solid solubility of iron in magnesium. *J. Inst. Met.* **1963**, *91*, 166–168.
14. Haitani, T.; Tamura, Y.; Motegi, T.; Kono, N.; Tamehiro, H. Solubility of Iron in Pure Magnesium and Cast Structure of Mg-Fe Alloy. *Mater. Sci. Forum* **2003**, *419–422*, 697–702. [[CrossRef](#)]
15. Yang, L.; Liu, G.; Ma, L.; Zhang, E.; Zhou, X.; Thompson, G. Effect of iron content on the corrosion of pure magnesium: Critical factor for iron tolerance limit. *Corros. Sci.* **2018**, *139*, 421–429. [[CrossRef](#)]
16. Xie, G.; Takada, H.; Kanetaka, H. Development of high performance MgFe alloy as potential biodegradable materials. *Mater. Sci. Eng. A* **2016**, *671*, 48–53. [[CrossRef](#)]
17. Vojtěch, D.; Čížová, H.; Volenec, K. Investigation of magnesium-based alloys for biomedical applications. *Kovove Mater.* **2006**, *44*, 211–223.
18. Zahiri, B.; Harrower, C.T.; Amirkhiz, B.S.; Mitlin, D. Rapid and reversible hydrogen sorption in Mg–Fe–Ti thin films. *Appl. Phys. Lett.* **2009**, *95*, 103114. [[CrossRef](#)]
19. Yoneda, Y.; Abe, H.; Ohshima, T.; Uchida, H. Phase transformation of Mg–Fe alloys. *J. Appl. Phys.* **2010**, *107*, 093505. [[CrossRef](#)]
20. Pandey, R.; Tekumalla, S.; Gupta, M. Magnesium-iron micro-composite for enhanced shielding of electromagnetic pollution. *Compos. Part B Eng.* **2019**, *163*, 150–157. [[CrossRef](#)]
21. Kabirian, F.; Mahmudi, R. Impression Creep Behavior of a Cast AZ91 Magnesium Alloy. *Met. Mater. Trans. A* **2009**, *40A*, 116–127. [[CrossRef](#)]
22. Blawert, C.; Hort, N.; Kainer, K.U. Automotive applications of magnesium and its alloys. *Indian Inst. Met.* **2004**, *57*, 397–408.
23. Luo, A.A. Recent Magnesium Alloy Development for Automotive Powertrain Applications. *Mater. Sci. Forum* **2003**, *419–422*, 57–66. [[CrossRef](#)]
24. Chen, J.; Bao, C.-G.; Liu, Z.-W.; Sun, B.-S.; Shu, Y.-C.; Li, Q.-K. Thermal properties of Mg-Al/AlN composites fabricated by powder metallurgy. *Acta Metall. Sinica* **2018**, *31*, 641–649. [[CrossRef](#)]
25. Choi, S.W.; Cho, H.S.; Kumai, S. Influence of precipitation on the coefficient of thermal expansion of Al-Si-Mg-Cu-(Ti) alloys. *J. Alloys Compd.* **2016**, *655*, 6–10. [[CrossRef](#)]
26. Uju, W.; Oguocha, I. A study of thermal expansion of Al–Mg alloy composites containing fly ash. *Mater. Des.* **2012**, *33*, 503–509. [[CrossRef](#)]
27. Mondal, A.; Kumar, S. Creep Behaviour of AE42 Magnesium Alloy and its Composites Using Impression Creep Technique. *Mater. Sci. Forum* **2010**, *638–642*, 1552–1557. [[CrossRef](#)]
28. Golmakaniyoon, S.; Mahmudi, R. Comparison of the effects of La- and Ce-rich rare earth additions on the microstructure, creep resistance, and high-temperature mechanical properties of Mg–6Zn–3Cu cast alloy. *Mater. Sci. Eng. A* **2011**, *528*, 5228–5233. [[CrossRef](#)]
29. Sankaranarayanan, S.; Sabat, R.; Jayalakshmi, S.; Suwas, S.; Gupta, M. Effect of nanoscale boron carbide particle addition on the microstructural evolution and mechanical response of pure magnesium. *Mater. Des.* **2014**, *56*, 428–436. [[CrossRef](#)]
30. Stanford, N.; Barnett, M. Effect of composition on the texture and deformation behaviour of wrought Mg alloys. *Scr. Mater.* **2008**, *58*, 179–182. [[CrossRef](#)]
31. Wu, B.; Zhao, Y.; Du, X.; Zhang, Y.; Wagner, F.; Esling, C. Ductility enhancement of extruded magnesium via yttrium addition. *Mater. Sci. Eng. A* **2010**, *527*, 4334–4340. [[CrossRef](#)]
32. Available online: <http://www.matweb.com/search/DataSheet.aspx?MatGUID=654ca9c358264b5392d43315d8535b7d> (accessed on 8 August 2021).
33. Avedesian, M.M.; Baker, H. *ASM Specialty Handbook: Magnesium and Magnesium Alloys*; ASM International: Novelt, OH, USA, 1999.
34. Huang, S.J.; Abbas, A.; Ballóková, B. Effect of CNT on microstructure, dry sliding wear and compressive mechanical properties of AZ61 magnesium alloy. *J. Mater. Res. Tech.* **2019**, *8*, 4273–4286. [[CrossRef](#)]
35. Dieter, G.E. *Mechanical Metallurgy, SI Metric Edition*; McGraw-Hill: New York, NY, USA, 1988.
36. Lloyd, D. Particle reinforced aluminium and magnesium matrix composites. *Intl. Mater. Rev.* **1994**, *39*, 1–23. [[CrossRef](#)]
37. Gupta, M.; Lai, M.; Saravananathan, D. Synthesis, microstructure and properties characterization of disintegrated melt deposited Mg/SiC composites. *J. Mater. Sci.* **2000**, *35*, 2155–2165. [[CrossRef](#)]

38. Hassan, S.; Gupta, M. Development of high performance magnesium nano-composites using nano-Al<sub>2</sub>O<sub>3</sub> as reinforcement. *Mater. Sci. Eng. A* **2005**, *392*, 163–168. [[CrossRef](#)]
39. Bauri, R.; Surappa, M.K. Processing and properties of Al-Li-SiCp composites. *Sci. Tech. Adv. Mater.* **2007**, *8*, 494–502. [[CrossRef](#)]
40. Hong, S.-J.; Kim, H.-M.; Huh, D.; Suryanarayana, C.; Chun, B.S. Effect of clustering on the mechanical properties of SiC particulate-reinforced aluminum alloy 2024 metal matrix composites. *Mater. Sci. Eng. A* **2003**, *347*, 198–204. [[CrossRef](#)]
41. Arsenault, R.J.; Shi, N.; Feng, C.R.; Wang, L. Localized deformation of SiC-Al composites. *Mater. Sci. Eng. A* **1991**, *131*, 55–68. [[CrossRef](#)]
42. Wang, Y.N.; Huang, J.C. The role of twinning and untwinning in yielding behavior in hot-extruded Mg–Al–Zn alloy. *Acta Mater.* **2007**, *55*, 897–905. [[CrossRef](#)]
43. Barnett, M.R. Twinning and the ductility of magnesium alloys: Part I: “Tension” twins. *Mater. Sci. Eng. A* **2007**, *464*, 1–7. [[CrossRef](#)]
44. Smithells, C.J.; Smith, C.S. *Metals Reference Book*, 5th ed.; Butterworth’s & Co. Ltd.: London, UK, 1976.
45. Jayalakshmi, S.; Sankaranarayanan, S.; Koh, S.; Gupta, M. Effect of Ag and Cu trace additions on the microstructural evolution and mechanical properties of Mg–5Sn alloy. *J. Alloys Compd.* **2013**, *565*, 56–65. [[CrossRef](#)]
46. Available online: [www.matweb.com](http://www.matweb.com) (accessed on 7 August 2021).
47. Sastry, D.H. Creep technique: An overview. *Mater. Sci. Eng. A* **2005**, *409*, 67–75. [[CrossRef](#)]
48. Thenambika, V.; Jayalakshmi, S.; Singh, R.; Nidhi, J.; Gupta, M. Impression Creep Behaviour of Extruded Mg–Sn Alloy. *Int. J. Veh. Struct. Syst.* **2016**, *8*, 174–178. [[CrossRef](#)]
49. Labib, F.; Mahmudi, R.; Ghasemi, H. Impression creep behavior of extruded Mg–SiCp composites. *Mater. Sci. Eng. A* **2015**, *640*, 91–97. [[CrossRef](#)]
50. Mordike, B.L.; Kainer, K.U.; Moll, F.; Sommer, B. *Magnesium Science and Technology*; Aghion, E., Eliezer, D.E., Eds.; Wiley-VCH: Weinheim, Germany, 1997; p. 178.
51. Moll, F.; Kainer, K.U.; Mordike, B.L. *Magnesium Alloys and Their Applications*; Mordike, B.L., Kainer, K.U., Eds.; Werkstoff-Informationsgesellschaft: Frankfurt, Germany, 1998; p. 647.
52. Maruyama, K.; Suzuki, M.; Sato, H. Creep strength of magnesium-based alloys. *Metall. Mater. Trans. A* **2002**, *33A*, 875–882. [[CrossRef](#)]
53. Peng, L.; Yang, F.; Nie, J.-F.; Li, J. Impression creep of a Mg–8Zn–4Al–0.5Ca alloy. *Mater. Sci. Eng. A* **2005**, *410–411*, 42–47. [[CrossRef](#)]
54. Kumar, H.; Chaudhari, G. Creep behavior of AS41 alloy matrix nano-composites. *Mater. Sci. Eng. A* **2014**, *607*, 435–444. [[CrossRef](#)]
55. Mesarovic, S.D. Dislocation Creep: Climb and Glide in the Lattice Continuum. *Crystals* **2017**, *7*, 243. [[CrossRef](#)]
56. Kassner, M.E. *Fundamentals of Creep in Metals and Alloys*, 3rd ed.; Butterworth-Heinemann: Waltham, MA, USA, 2005.
57. Chawla, N.; Chawla, K.K. *Metal Matrix Composites*; Springer: New York, NY, USA, 2006.
58. Sankaranarayanan, S.; Sabat, R.; Jayalakshmi, S.; Suwas, S.; Gupta, M. Microstructural evolution and mechanical properties of Mg composites containing nano-B<sub>4</sub>C hybridized micro-Ti particulates. *Mater. Chem. Phys.* **2014**, *143*, 1178–1190. [[CrossRef](#)]
59. *Mechanical Properties of Niobium and Alloys Versus Temperature, Materials Data Sheet*; Cabot Corporation Homepage: Boyertown, PA, USA; Available online: <http://www.cabot-corp.com> (accessed on 8 August 2021).
60. Arsenault, R. Particulate microstructure of fiber and SiC in 6061 Al composites. *Scripta Metall.* **1983**, *71*, 67–71. [[CrossRef](#)]
61. Brown, L.M.; Stobbs, W.M. The work-hardening of copper-silica v. equilibrium plastic relaxation by secondary dislocations. *Philos. Mag.* **1976**, *34*, 351–372. [[CrossRef](#)]
62. Miller, W.; Humphreys, F. Strengthening mechanisms in particulate metal matrix composites. *Scr. Met. Mater.* **1991**, *25*, 33–38. [[CrossRef](#)]
63. Nardone, V.; Prewo, K. On the strength of discontinuous silicon carbide reinforced aluminium composites. *Scripta Metall.* **1986**, *20*, 43–48. [[CrossRef](#)]
64. Zhang, Z.; Chen, D.L. Consideration of Orowan strengthening effect in particulate-reinforced metal matrix nanocomposites: A model for predicting their yield strength. *Scr. Mater.* **2006**, *54*, 1321–1326. [[CrossRef](#)]
65. Seensattayawong, P.; Pandee, P.; Limmaneevichitr, C. Impression creep properties of hypoeutectic Al–Si alloys with scandium additions. *Mater. Today Proc.* **2018**, *5*, 9440–9446. [[CrossRef](#)]
66. Haghshenas, M.; Gupta, M. Magnesium nanocomposites: An overview on time-dependent plastic (creep) deformation. *Def. Technol.* **2018**, *15*, 123–131. [[CrossRef](#)]